CrystEngComm

ROYAL SOCIETY OF CHEMISTRY

PAPER

View Article Online
View Journal | View Issue

Check for updates

Cite this: *CrystEngComm*, 2025, **27**, 7032

Structural adaptation in a cadmium–porphyrin MOF through solvent-driven change of interpenetration

Michelle Ernst *[a] and Tomasz Poręba *[b]

Cadmium–porphyrin metal–organic frameworks combine the structural rigidity of the porphyrin core with the coordination flexibility of closed-shell Cd^{2+} centres, enabling diverse framework topologies and versatile applications. Here, we report a single-crystal-to-single-crystal transformation in a $CdCl_2$–*meso*-tetra(4-pyridyl)porphyrin (H_2TPyP) MOF induced by mild thermal desolvation (120 °C in air). The solvated MOF (UB-MOF-1) adopts a non-interpenetrated $CdSO_4$-type topology stabilized by 1,1,2,2-tetrachloroethane and 3-chloroaniline guests. Upon solvent removal, the framework undergoes irreversible drastic rearrangement to a two-fold interpenetrated cds-type network (ESRF-MOF-1), accompanied by more than a twofold reduction in accessible pore volume. Periodic DFT calculations show that, while guest inclusion substantially stabilizes the open framework UB-MOF-1, the interpenetrated, solvent-free ESRF-MOF-1 is thermodynamically favoured over the hypothetical empty UB-MOF-1 as interpenetration provides even greater stabilization. The transformation, driven by framework densification, is irreversible due to geometric pore constraints. This study demonstrates how controlled solvent manipulation can trigger topology changes in porphyrin-based MOFs, offering a route to design dense, structurally locked architectures with tailored accessibility.

Received 20th August 2025,
Accepted 1st October 2025

DOI: 10.1039/d5ce00815h

rsc.li/crystengcomm

Open Access Article. Published on 02 October 2025. Downloaded on 1/28/2026 2:35:32 PM.
This article is licensed under a Creative Commons Attribution 3.0 Unported Licence.

Introduction

Cadmium–porphyrin coordination networks combine the intrinsic stability and rigidity of the porphyrin core with the flexible coordination preferences of closed-shell d^{10} Cd(II) centres, enabling the formation of a wide variety of stable structural motifs. Tetratopic ligands such as *meso*-tetra(4-pyridyl)porphyrin (H_2TPyP) are particularly well suited for constructing extended three-dimensional frameworks with diverse topologies and mechanical properties. The structural diversity achievable with these building blocks has been widely documented, including non-interpenetrated, interpenetrated, and layered architectures. Potential applications of cadmium–porphyrin frameworks include gas sorption, fluorescence sensing, catalysis, and studies of mechanical responsiveness,[1–5] although the toxicity of cadmium might limit their practical use in some technological contexts.

Metal–organic frameworks (MOFs) represent a broader class of coordination polymers characterized by their permanent porosity and crystalline order. They have received ongoing attention due to their structural richness and potential for tuneable porosity and functionality. In this study, we explore solvent-assisted structural changes in two related Cd–porphyrin-based MOFs.

Previous work has highlighted the structural adaptability and solvent-responsive behaviour of Cd–TPyP MOFs. Subtle changes, such as metal type, synthetic conditions, recrystallization method, and guest inclusion can significantly influence the dimensionality, degree of interpenetration, and porosity of these porphyrinic coordination networks.[6] Several 3D Cd–TPyP MOFs have been reported, featuring interpenetrated networks and remarkable coordination diversity: individual porphyrin ligands were observed to bind one, two, four, or five (through porphyrin metalation) cadmium centres, while Cd^{2+} nodes exhibited five distinct coordination geometries with various supramolecular architectures.[6,7] For example, combining freebase or partially metalated TPyP with CdI_2 subjected to a solvent-diffusion crystallization process yields layered, solvated coordination polymers that accommodated multiple tetrachloroethane molecules between porphyrin layers.[8] This suggests that solvent inclusion during crystallization contributes to the thermodynamic stabilization of these layered structures in the solid state. In contrast, HMOF-1, a non-interpenetrated, solvent-free CdI_2–TPyP framework (crystallized under similar conditions) displays a 3D hinged "lattice-fence" topology with extraordinary anisotropic

[a] *Institute of Geological Sciences, University of Bern, 3012 Bern, Switzerland. E-mail: michelle.ernst@unibe.ch*
[b] *Laboratory for Quantum Magnetism, Institute of Physics, École Polytechnique Fédérale de Lausanne, Lausanne CH-1015, Switzerland. E-mail: tomasz.poreba@epfl.ch*

This journal is © The Royal Society of Chemistry 2025

Open Access Article. Published on 02 October 2025. Downloaded on 1/28/2026 2:35:32 PM. This article is licensed under a Creative Commons Attribution 3.0 Unported Licence.

reversible thermal expansion.[5] This phenomenon was attributed to the large hinge-like motion range around the Cd centres within the framework.†

By contrast, despite having a similar van der Waals ligand radius, $Cd(SH)_2(H_2TPyP)$ crystallized under hydrothermal conditions forms an interpenetrated, solvent-free, **cds**-type MOF and not flexible hinged structure.[7] These examples highlight the remarkable structural diversity of Cd–TPyP MOFs, even when built from the same ligands, as a result of different synthetic and crystallization pathways. In this work, we present an alternative post-synthetic route to modify the framework packing: thermal activation removes the solvent molecules and induces an increase in the degree of interpenetration.

Changes in the degree of interpenetration upon solvent removal have been widely observed across a broad range of MOF systems.[9] Transformations from non-interpenetrated to interpenetrated structures have been reported in multiple studies, demonstrating the role of solvent molecules in stabilizing non-interpenetrated frameworks and the tendency of the framework to collapse into a denser interpenetrated structure once these molecules are removed.[10–15]

In many cases, increases in the degree of interpenetration have been observed, such as two-fold to three-fold[16,17] and two-fold to four-fold,[18] as well as more complex transitions including four-fold to five-fold,[19] five-fold to six-fold,[20] and even seven-fold to eight-fold.[21] This highlights the general tendency of interpenetration to increase as solvent molecules are removed and structural relaxation occurs. In contrast, transformations to a lower degree of interpenetration are exceedingly rare, and, we are not aware of any examples of transformations that decrease the degree of interpenetration upon simple solvent removal; instead, reported cases involve reactions leading to deinterpenetration,[22,23] interpenetration increases induced by guest addition,[24] or even reversible interpenetration changes triggered by solvent exchange.[25]

In this context, understanding why and how guest removal can trigger such radical topological rearrangements is essential for the rational design of adaptive and responsive materials. The ability to rationalize and predict interpenetration transitions remains a central goal in crystal engineering, with direct implications for designing MOFs that combine functionality with stability, porosity, and dynamic behaviour in targeted ways.

Methods

Synthetic procedures

The synthesis of the precursor *catena*-[(μ-5,10,15,20-tetrakis(pyridin-4-yl)porphyrin)-dichloro-cadmium(II)] solvated with 1,1,2,2-tetrachloroethane (TCE) and 3-chloroaniline herein named UB-MOF-1 was described by us elsewhere (CCDC 2157164),[26] and the synthesis essentially follows the procedure described by DeVries *et al.*[5] To obtain a non-solvated MOF, the single-crystal of UB-MOF-1 was placed in a laboratory dryer directly on a goniometer head at 120 °C for 4 hours in air.

Structure determination

Subsequently, the single crystal with approximate dimensions of 0.075 mm × 0.045 mm × 0.030 mm was cooled down to room temperature in a desiccator over silica gel. The single-crystal X-ray diffraction (SC-XRD) experiment was carried out on that crystal at the ID15B beamline at ESRF, using a convergent monochromatic beam (0.4099 Å). Data were collected at room temperature. The data collection strategy consisted of a single ω-scan ($-70° \leq \omega \leq +70°$), with 0.5° step width and 0.5 s exposure time. The preliminary data reduction has been carried out in the CrysAlis Pro software.[27] The structure was solved with the dual-space algorithm, as implemented in SHELXT.[28] All non-hydrogen atoms were refined anisotropically using the full-matrix, least-squares method on F^2 in the SHELXL software (*cf.* Table 1).[29] The hydrogen atoms were located in a difference Fourier map, and then refined using the riding model. Isotropic displacement factors of hydrogen atoms were equal to 1.2 times the value of the displacement factor of the parent atoms. CCDC 2480007 contains the supplementary

Table 1 Selected crystallographic parameters and structure refinement data for ESRF-1

Empirical formula	$C_{40}H_{26}CdCl_2N_8$
Formula weight	801.99
Temperature/K	298(1)
Crystal system	Orthorhombic
Space group	*Pnna*
a/Å	12.8121(2)
b/Å	15.6630(2)
c/Å	20.3134(4)
α/°	90
β/°	90
γ/°	90
Volume/Å^3	4076.41(11)
Z	4
ρ_{calc} g cm^{-3}	1.307
μ/mm^{-1}	0.729
F(000)	1616.0
Crystal size/mm^3	0.1 × 0.05 × 0.04
Radiation	Synchrotron (λ = 0.40988)
2Θ range for data collection/°	3.31 to 29.686
Index ranges	$-15 \leq h \leq 16$, $-19 \leq k \leq 19$, $-21 \leq l \leq 25$
Reflections collected	15 493
Independent reflections	4070 [R_{int} = 0.0463, R_{sigma} = 0.0680]
Data/restraints/parameters	4070/0/234
Goodness-of-fit on F^2	1.129
Final *R* indexes [$I \geqq 2\sigma(I)$]	R_1 = 0.0675, wR_2 = 0.2276
Final *R* indexes [all data]	R_1 = 0.0739, wR_2 = 0.2327
Largest diff. peak/hole/e Å^{-3}	1.31/−0.54

† Even though, the unit cell dimensions are very close to the ones found for the MOF reported in this study ($CdCl_2$–TPyP), the reported structure crystallizes in an orthorhombic space group with β = 90° and a "hinge angle" between the vector connecting the axial ligands of Cd and a plane of TPyP around 26.7°, while our structure adopts a monoclinic cell with β = 93.5°, with a hinge angle of 43.5°.

Open Access Article. Published on 02 October 2025. Downloaded on 1/28/2026 2:35:32 PM. This article is licensed under a Creative Commons Attribution 3.0 Unported Licence.

crystallographic data for this paper. The pore analysis has been carried out in PoreBlazer implemented as a Pore Analyser module in the CCDC Mercury software.[30] The calculations were performed using default settings: helium probe sigma of 2.58 Å (ε = 10.22 K), cut-off distance of 12.8 Å and grid size of 0.2 Å. Topological analysis of the structure was carried out in ToposPro v.5.5.3.1.[31]

Computational methods

All calculations were carried out using CP2K version 2024.3. Geometry optimizations were performed on the solvent-free frameworks of UB-MOF-1 and ESRF-MOF-1 and the filled UB-MOF-1, optimizing only the atomic coordinates while keeping the unit cell parameters fixed. The resulting structures show only minor deviations from the experimental models (*cf.* Fig. S1 in the SI). The Perdew–Burke–Ernzerhof (PBE) functional was employed with Grimme's D3(BJ) dispersion correction to account for van der Waals interactions. The DZVP-MOLOPT-SR-GTH basis set was used in combination with GTH pseudopotentials, and a plane-wave cutoff of 600 Ry was applied.

The binding energy E^{bind} of UB-MOF-1 corresponds to the sum of the electronic interaction energy of the framework with the solvent molecules plus the reorganization energy (*cf.* eqn (1)).

$$E^{\text{bind}} = E^{\text{filled}} - (E^{\text{empty}} + E^{\text{solvent}}) \quad (1)$$

This value was obtained by optimizing the pristine, solvent-containing UB-MOF-1, along with separate optimizations of the emptied framework and the isolated solvent molecules.

Results and discussion

Structural characterisation

The structure of a 2D coordination polymer containing both CdI_2 nodes and $H_2$4TPyP was first reported by Krishnamohan Sharma *et al.*[32] The synthesis was carried out in a 3 : 1 TCE–MeOH solution of $H_2$4TPyP layered with metal salts dissolved in MeOH. The layers of the resulting MOF are intercalated with TCE molecules in a 1 : 2 molar ratio. A similar synthesis was reported by DeVries in which $H_2$4TPyP was likewise dissolved in 3 : 1 TCE–MeOH, layered with 3-chloroaniline, and finally topped with a *N*,*N*′-dimethylacetamide solution of CdI_2. In this case, a **cds**-type solvent-free MOF was obtained. Although we carefully followed the synthetic procedure of DeVries[5] that yielded the **cds**-type solvent-free MOF (CCDC 854909), we obtained a solvated MOF (UB-MOF-1) containing both TCE and 3-CA. Moreover, the CdI_2 clusters in the framework were replaced by $CdCl_2$ ones. The non-incorporation of iodine in this structure has been previously attributed to competing Finkelstein-type halide exchange reaction with excess of the TCE, as discussed in our earlier work.[26]

Heating of UB-MOF-1 in air at 120 °C for 4 hours resulted in a fully emptied MOF (ESRF-MOF-1). Remarkably, the mild conditions for the desorption process resulted in single-crystal to single-crystal (SC–SC) transition, which allowed for subsequent SC-XRD structural determination. The integrity of the crystal is retained despite the drastic structural changes upon solvent removal (Fig. 1 and S2). Both structures, UB-MOF-1 and ESRF-MOF-1, are built of $CdCl_2$ *trans*-octahedral clusters bound together by tetradentate *meso*-tetra(4-pyridyl) porphyrin ($H_2$4TPyP) ligands.

However, topological analysis revealed significant differences between the two extended structures. In both cases, the Cd nodes and porphyrin cores function as square-planar four-connected units. The solvated UB-MOF-1 is an example of a $CdSO_4$-type net, where guest 1,1,2,2-tetrachloroethane is sandwiched between the porphyrin rings, and 3-chloroaniline occupies the interstitial voids (Fig. 1a and b). On the other hand, the emptied MOF, ESRF-MOF-1, forms a much more compact structure made of two interpenetrating identical **cds** nets (Fig. 1c and d).

The nodes of the net are shifted by 1/2*a*, 1/2*b* and 0.150*c* with respect to each other. As a result of the tight interpenetration, the structure of ESRF-MOF-1 is much denser than the theoretical solvent-free UB-MOF-1 (1.307 and 0.965 g cm^{-3}, respectively) and shows nearly half of the network-accessible helium volume (29.8% *versus* 55.1%).

The closed-shell electronic structure of Cd allows for certain structural flexibility around the metal centres, which can be noted as a "wavy" pattern (Fig. 1a) formed by the

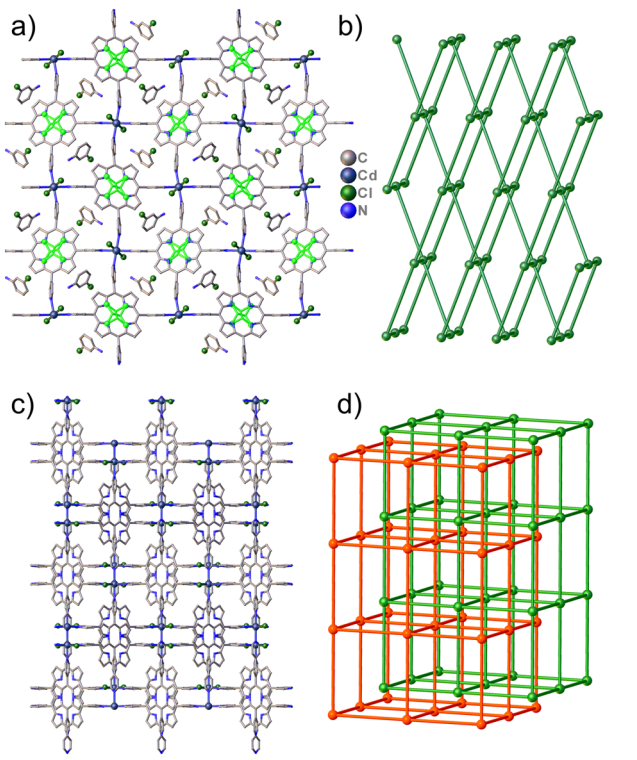

Fig. 1 Crystal structures ([100] view) and topological representations for UB-MOF-1 (a and b) and ESRF-MOF-1 (c and d), respectively. Hydrogens are omitted and TCE molecules sitting atop the porphyrin rings are depicted in bright green for clarity.

 This journal is © The Royal Society of Chemistry 2025

Open Access Article. Published on 02 October 2025. Downloaded on 1/28/2026 2:35:32 PM. This article is licensed under a Creative Commons Attribution 3.0 Unported Licence.

cadmium clusters bonded to the pyridin-4-yl ligand at 9.3(2)°. This feature combined with the rigidity of the porphyrin linkers likely allows for the controlled release of both solvents (TCE and 3-CA) before the structure collapse into the interpenetrated net. Noteworthy, at the applied annealing conditions (120 °C, 1 atm) both solvents reach relatively high vapour pressure, which fosters their full desorption (~370 mmHg and ~25 mmHg for TCE and 3-CA respectively, estimated from Antoine coefficients).[33,34]

On the other hand, even though the maximum pore diameter differs only slightly between the two structures (4.68 Å in UB-MOF-1 and 4.37 Å in ESRF-MOF-1), the latter could not be reversed back to the solvated form. Attempts to restore the solvated phase by immersing ESRF-MOF-1 in a 1% w/w 3-chloroaniline solution in MeOH for 3 hours at room temperature were unsuccessful. Similarly, incorporation of EtOH, MeOH and H_2O by the same technique were unsuccessful, as evidenced by the subsequently collected XRD data (Table S2). The reason for this behaviour likely lies in the small pore limiting diameter, the narrowest constriction along the pore channel, of ESRF-MOF-1 of 1.34 Å (3.1 Å in UB-MOF-1), which does not allow for molecules larger than He to penetrate the crystal interior. Analysis of the residual electron density in the structure, performed using the PLATON SQUEEZE module,[35] indicates 100 residual electrons in the voids per unit cell. Since there are four voids, each contains 25 electrons, which corresponds to ~0.4 3-chloroaniline molecules per void. Modelling of this residual density does not reveal any connected network that would resemble (partially) ordered 3-CA or TCE molecules. Nonetheless, we cannot exclude the possibility that the MOF is not fully desolvated, with some remaining guests disordered beyond the resolution limit. The residual density is likely not due to TCE, given its much lower evaporation point, as discussed above.

Thermodynamic analysis

The binding energy of UB-MOF-1 with its solvent guests (two TCE and four 3-CA molecules per unit cell) calculated with periodic DFT shows a substantial stabilization by guest inclusion of −765.6 kJ mol^{-1} (*cf.* Table S1 in the SI). Upon heating, these guests are expelled from the pores, allowing the framework to relax into a more compact and energetically favoured interpenetrated topology. Periodic DFT further shows that the interpenetrated ESRF-MOF-1 is more stable (−112.8 kJ mol^{-1} per unit cell) than the hypothetical, solvent-free UB-MOF-1 structure (*cf.* Table S1 in SI), providing strong evidence that interpenetration is energetically favourable following the solvent removal. Although the energy gain from lattice reorganization (−112.8 kJ mol^{-1}) is much smaller than the stabilization provided by the solvent inclusion (−765.6 kJ mol^{-1}), the transformation remains irreversible under the conditions tested. This conclusion still holds when partial guest removal is considered, consistent with the residual electron density observed in the pores. To account for this, we also modelled the solvent interaction energy for a partially desolvated case (see Table S1 SI) to be −458.1 kJ mol^{-1}. Instead, the irreversible nature of the transition is dictated by the geometry: the interpenetrated structure imposes steric constraints that prevent the reuptake of solvent molecules into the pores, as discussed above.

For comparison, cluster-based interaction energies between UB-MOF-1 and the guest solvent molecules yielded values of −114.5 kJ mol^{-1} for TCE and −124.6 kJ mol^{-1} for 3-CA.[26] This corresponds to an interaction energy of −727.4 kJ mol^{-1} per unit cell ($CdCl_2(4TPyP)_2{\cdot}C_2H_2Cl_4{\cdot}2C_6H_4NH_2Cl$, $Z' = 0.5$, $Z = 2$). The close agreement between the cluster-based values and our periodic calculations is reassuring.

Solvent removal as a trigger for interpenetration

The transformation from the non-interpenetrated UB-MOF-1 to the interpenetrated ESRF-MOF-1 framework is induced by thermal desolvation at relatively mild conditions (120 °C in air). This behaviour is consistent with a broader pattern observed in MOFs, where solvent molecules help to stabilize open frameworks, and their removal leads to framework collapse or contraction into a much denser phase.[36–41] In our case, it leads to the transition from a $CdSO_4$-type topology to a two-fold interpenetrated **cds** net. This rearrangement, achieved *via* cleavage and reformation of coordination bonds, mirrors many reported examples in the literature where the degree of interpenetration increases upon desolvation. The resulting denser framework reflects a drive to minimize void space and maximize intermolecular interactions in the absence of guests. In addition to enthalpic considerations, entropic contributions may also play a role: the release of solvent molecules is an entropic gain, and interpenetrated configurations are statistically more probable because there are more ways to intertwine identical networks than to keep them fully separated.

Our periodic DFT calculations underline the thermodynamic driving force of this transformation. The interpenetrated ESRF-MOF-1 framework is calculated to be 112.8 kJ mol^{-1} per unit cell more stable than the hypothetical empty non-interpenetrated UB-MOF-1, consistent with the experimentally observed transformation. While the solvated UB-MOF-1 is stabilized by a strong interaction energy between the framework and the guest solvent molecules (765.6 kJ mol^{-1} per unit cell), this interaction is lost upon desolvation, prompting the framework to irreversibly reorganize into a more energetically favourable and compact topology.

It is difficult to generally estimate the influence of the framework–solvent interaction strength on the formation of interpenetrated networks due to different ways XRD structural data is treated before publishing.[42] CSD v.5.44 contains 108 881 entries which can be classified as metal–organic frameworks and/or coordination polymers (search criteria: contains transition metal, contains "*catena*" keyword,

Open Access Article. Published on 02 October 2025. Downloaded on 1/28/2026 2:35:32 PM. This article is licensed under a Creative Commons Attribution 3.0 Unported Licence.

3D structure determined), whereas in nearly 11% of them a disordered part of a molecule and/or solvent have been removed using the PLATON SQUEEZE routine[35] (11 971 entries, keyword "SQUEEZE"). In some cases, by omitting the solvent molecules one may obscure the underlying activation phenomena. For example, in the isostructural iodine analogue of ESRF-MOF-1, HMOF-1,[5] the bending around the Cd node has been identified to be responsible for the highly anisotropic thermal expansion (without increase of the degree of interpenetration). However, the reported results of the elemental analysis (in the SI of the cited work) indicate the presence of impurities and/or residual solvent, which has been eliminated from the reported crystal structure using the SQUEEZE routine. In this case, the source of such high structural mobility without the increase of degree of interpenetration might lie in the phase transition associated with the solvent removal. In fact, the collected X-ray powder diffractograms for this compound show splitting of certain Bragg reflections above 300 K.

Irreversibility of the transformation due to reduced pore access

Following the SC–SC transformation and interpenetration, ESRF-MOF-1 retains a similar overall pore volume to UB-MOF-1, but the pore accessibility is markedly reduced (Fig. S4). While the maximum pore diameters remain comparable (4.68 Å in UB-MOF-1 *vs.* 4.37 Å in ESRF-MOF-1), the pore limiting diameter, the narrowest constriction controlling guest entry, drops substantially from 3.1 Å to 1.34 Å. This geometric constraint effectively blocks the re-entry of solvent molecules or larger guests into the interpenetrated framework.

Attempts to reverse the transformation by re-soaking the ESRF-MOF-1 crystals in solutions of 3-chloroaniline, ethanol, methanol (also at 50 °C, see Fig. S3), and water failed, highlighting the irreversibility of the transition under mild conditions (Table S2). Once the interpenetrated structure forms, its narrow channels prevent diffusion of new guest molecules, thus trapping the framework in a dense, closed-pore state. In this sense, the transformation is not simply temperature-dependent, but accessibility-limited, and ESRF-MOF-1 behaves more like an "exhale" MOF than a breathing one.[37]

Conclusions

We have shown that thermal desolvation of a cadmium–porphyrin MOF induces a single-crystal-to-single-crystal transformation from a non-interpenetrated to a two-fold interpenetrated network. This structural rearrangement is energetically favoured and leads to irreversible loss of guest accessibility due to reduced pore entry dimensions. Although the material does not exhibit dynamic behaviour such as breathing or switching, it highlights how solvent molecules play a key role in stabilizing open framework architectures. Their removal can drive the system toward denser, more stable configurations, including the formation of interpenetrated networks. This underscores the potential of controlled solvent manipulation as a design tool in the crystal engineering of structurally responsive yet robust MOFs.

Conflicts of interest

There are no conflicts to declare.

Data availability

Supplementary information: the supplementary information (SI) contains details on the geometry optimization, periodic DFT results, solvent desorption and crystal appearance, solvent reabsorption experiments, visualization of structural voids. See DOI: **https://doi.org/10.1039/D5CE00815H**.

The structural data supporting the findings of this study are available in the Cambridge Crystallographic Data Centre (CCDC): CCDC 2480007 contains the supplementary crystallographic data for this paper.[43]

All computation files are openly available in the Materials Cloud Archive under **https://doi.org/10.24435/materialscloud:ja-j4**.

Acknowledgements

We thank Dr. Lars Gnägi and Dr. Georgia Cametti for their technical assistance during sample preparation and initial XRD characterization. We acknowledge the European Synchrotron Radiation Facility (ESRF) for provision of synchrotron radiation facilities under proposal number HC-4862 and we would like to thank Dr. Davide Comboni for assistance and support in using beamline ID15b. The authors are thankful for the allocation of computing resources from the Swiss National Supercomputing Centre (CSCS) under project ID uzh1.

Notes and references

1 Q. Li, Y. Luo, Y. Ding, Y. Wang, Y. Wang, H. Du, R. Yuan, J. Bao, M. Fang and Y. Wu, *Dalton Trans.*, 2019, **48**, 8678–8692.
2 H. M. Tay, E. J. Goddard and C. Hua, *CrystEngComm*, 2022, **24**, 7277–7282.
3 C. Pereira, M. Simões, J. Tomé and F. Almeida Paz, *Molecules*, 2016, **21**, 1348.
4 C. Wang, D. Ding, X. Jiang and B. Zhou, *J. Anal. Chem.*, 2021, **76**, 772–778.
5 L. D. DeVries, P. M. Barron, E. P. Hurley, C. Hu and W. Choe, *J. Am. Chem. Soc.*, 2011, **133**, 14848–14851.
6 L. D. DeVries and W. Choe, *J. Chem. Crystallogr.*, 2009, **39**, 229–240.
7 N. Zheng, J. Zhang, X. Bu and P. Feng, *Cryst. Growth Des.*, 2007, **7**, 2576–2581.
8 C. V. K. Sharma, G. A. Broker, J. G. Huddleston, J. W. Baldwin, R. M. Metzger and R. D. Rogers, *J. Am. Chem. Soc.*, 1999, **121**, 1137–1144.
9 M. Gupta and J. J. Vittal, *Coord. Chem. Rev.*, 2021, **435**, 213789.

 This journal is © The Royal Society of Chemistry 2025

Open Access Article. Published on 02 October 2025. Downloaded on 1/28/2026 2:35:32 PM. This article is licensed under a Creative Commons Attribution 3.0 Unported Licence.

10 S. B. Choi, H. Furukawa, H. J. Nam, D. Jung, Y. H. Jhon, A. Walton, D. Book, M. O'Keeffe, O. M. Yaghi and J. Kim, *Angew. Chem.*, 2012, **124**, 8921–8925.
11 H. Aggarwal, P. Lama and L. J. Barbour, *Chem. Commun.*, 2014, **50**, 14543–14546.
12 P. Shen, W. W. He, D. Y. Du, H. L. Jiang, S. L. Li, Z. L. Lang, Z. M. Su, Q. Fu and Y. Q. Lan, *Chem. Sci.*, 2014, **5**, 1368–1374.
13 S. Jeong, D. Kim, J. Park, S. Shin, H. Kim, G. H. Jeong, D. Moon, H. R. Moon and M. S. Lah, *Chem. Mater.*, 2017, **29**, 3899–3907.
14 A. Ferguson, L. Liu, S. J. Tapperwijn, D. Perl, F. X. Coudert, S. Van Cleuvenbergen, T. Verbiest, M. A. Van Der Veen and S. G. Telfer, *Nat. Chem.*, 2016, **8**, 250–257.
15 L. Robison, X. Gong, A. M. Evans, F. A. Son, X. Wang, L. R. Redfern, M. C. Wasson, Z. H. Syed, Z. Chen, K. B. Idrees, T. Islamoglu, M. Delferro, W. R. Dichtel, F. X. Coudert, N. C. Gianneschi and O. K. Farha, *J. Am. Chem. Soc.*, 2021, **143**, 1503–1512.
16 H. Aggarwal, P. M. Bhatt, C. X. Bezuidenhout and L. J. Barbour, *J. Am. Chem. Soc.*, 2014, **136**, 3776–3779.
17 H. Aggarwal, R. K. Das, P. M. Bhatt and L. J. Barbour, *Chem. Sci.*, 2015, **6**, 4986–4992.
18 S. Gao, R. Q. Fan, X. M. Wang, L. G. Wei, Y. Song, X. Du, K. Xing, P. Wang and Y. L. Yang, *Phys. Chem. Chem. Phys.*, 2016, **18**, 19001–19010.
19 M. Ming, Q. Chen and J. Chen, *J. Solid State Chem.*, 2020, **285**, 121236.
20 J. P. Zhang, Y. Y. Lin, W. X. Zhang and X. M. Chen, *J. Am. Chem. Soc.*, 2005, **127**, 14162–14163.
21 Z. Chen, G. Gallo, V. A. Sawant, T. Zhang, M. Zhu, L. Liang, A. Chanthapally, G. Bolla, H. S. Quah, X. Liu, K. P. Loh, R. E. Dinnebier, Q. Xu and J. J. Vittal, *Angew. Chem.*, 2020, **132**, 843–848.
22 M. K. Bellas, J. J. Mihaly, M. Zeller and D. T. Genna, *Inorg. Chem.*, 2017, **56**, 950–955.
23 C. Y. Heo, M. L. Díaz-Ramírez, S. H. Park, M. Kang, C. S. Hong and N. C. Jeong, *ACS Appl. Mater. Interfaces*, 2024, **16**, 9068–9077.
24 D. Yan, Y. Chen, Y. Yang, Z. Guo and J. Guo, *Inorg. Chem.*, 2022, **61**, 1360–1367.
25 Y. Wang, S. S. Meng, P. X. Lin, Y. W. Xiao, Q. Q. Ma, Q. Xie, Y. Y. Chen, X. J. Zhao and J. Chen, *Inorg. Chem.*, 2016, **55**, 4069–4071.
26 M. Ernst, T. Poręba, L. Gnägi and G. Gryn'ova, *J. Phys. Chem. C*, 2023, **127**, 523–531.
27 *CrysAlis PRO*, Agilent Technologies Ltd, Yarnton, Oxfordshire, England, 2014.
28 G. M. Sheldrick, *Acta Crystallogr., Sect. A: Found. Adv.*, 2015, **71**, 3–8.
29 G. M. Sheldrick, *Acta Crystallogr., Sect. C: Struct. Chem.*, 2015, **71**, 3–8.
30 C. F. Macrae, I. Sovago, S. J. Cottrell, P. T. A. Galek, P. McCabe, E. Pidcock, M. Platings, G. P. Shields, J. S. Stevens, M. Towler and P. A. Wood, *J. Appl. Crystallogr.*, 2020, **53**, 226–235.
31 V. A. Blatov, A. P. Shevchenko and D. M. Proserpio, *Cryst. Growth Des.*, 2014, **14**, 3576–3586.
32 C. V. Krishnamohan Sharma, G. A. Broker and R. D. Rogers, *J. Solid State Chem.*, 2000, **152**, 253–260.
33 J. Polak, S. Murakami, V. T. Lam and G. C. Benson, *J. Chem. Eng. Data*, 1970, **15**(2), 323–328.
34 A. A. Zalikin, V. L. Kochetkov and Yu. A. Strepikheev, *Khim. Prom.*, 1965, **41**, 338.
35 A. L. Spek, *Acta Crystallogr., Sect. C: Struct. Chem.*, 2015, **71**, 9–18.
36 M. de J. Velásquez-Hernández, V. B. López-Cervantes, E. Martínez-Ahumada, M. Tu, U. Hernández-Balderas, D. Martínez-Otero, D. R. Williams, V. Martis, E. Sánchez-González, J.-S. Chang, J. S. Lee, J. Balmaseda, R. Ameloot, I. A. Ibarra and V. Jancik, *Chem. Mater.*, 2022, **34**, 669–677.
37 G. Férey and C. Serre, *Chem. Soc. Rev.*, 2009, **38**, 1380–1399.
38 K. Maity, V. Bon and S. Kaskel, *Chem. Mater.*, 2023, **35**, 4192–4200.
39 B. Manna, S. Singh and S. K. Ghosh, *J. Chem. Sci.*, 2014, **126**, 1417–1422.
40 S. Chen, Z. Zhang, W. Chen, B. E. G. Lucier, M. Chen, W. Zhang, H. Zhu, I. Hung, A. Zheng, Z. Gan, D. Lei and Y. Huang, *Nat. Commun.*, 2024, **15**, 10776.
41 R. Scatena, Y. T. Guntern and P. Macchi, *J. Am. Chem. Soc.*, 2019, **141**, 9382–9390.
42 T. Poręba, P. Macchi and M. Ernst, *Nat. Commun.*, 2022, **13**, 5288.
43 CCDC 2480007: Experimental Crystal Structure Determination, 2025, DOI: **10.5517/ccdc.csd.cc2p7n7v**.